

Article

Pyridinyl Conjugate of UiO-66-NH₂ as Chemosensor for the Sequential Detection of Iron and Pyrophosphate Ion in Aqueous Media

Aasif Helal ^{1,*} , Md. Eyasin Arafat ¹  and Mohammad Mizanur Rahman ² 

¹ Center of Research Excellence in Nanotechnology, King Fahd University of Petroleum and Minerals, Dhahran 31261, Saudi Arabia; g201707550@kfupm.edu.sa

² Center of Research Excellence in Corrosion, King Fahd University of Petroleum and Minerals, Dhahran 31261, Saudi Arabia; mrahman@kfupm.edu.sa

* Correspondence: aasifh@kfupm.edu.sa; Tel.: +966-013-860-7532

Received: 7 October 2020; Accepted: 23 November 2020; Published: 30 November 2020



Abstract: A new chemosensor UiO-66-N-Py (Py = 2-methinepyridine, N = imine nitrogen) based on isorecticular UiO-66 (University of Oslo) Metal–Organic Framework (MOF) containing 2-methinepyridine functionalized organic linker was solvothermally synthesized and characterized. This UiO-66-N-Py was very selective and sensitive for detecting the Fe³⁺ ion and sequential detection of the pyrophosphate (PPi) anion. The limits of detection for the Fe³⁺ ion and PPi were calculated to be 10 ppb (0.19 μM) and 50 ppb (0.3 μM), respectively. The quenching constant K_{sv} for Fe³⁺ and the binding constant for PPi were $1.4 \times 10^5 \text{ M}^{-1}$ and $1.7 \times 10^5 \text{ M}^{-1}$, respectively. The functionalization of UiO-66-NH₂ with 2-methinepyridine enhanced its fluorescence emission properties and introduced more binding sites for the analytes. We additionally studied the interaction of the sensor and the analytes with Fourier-transform infrared spectroscopy (FTIR), X-ray photoelectron spectroscopy (XPS), and Inductively Coupled Plasma Mass Spectrometry (ICP-MS). This chemosensor also demonstrated a regenerative emission property without loss in the detection ability for six consecutive cycles.

Keywords: chemosensor; emission; fluorescence; isorecticular; Metal–Organic Framework; sequential

1. Introduction

The selective sensing of heavy and transitional metals has attracted immense interest due to their considerably important structural, regulatory, and catalytic role in different biological systems. Among them, iron is vital, as it plays a very significant role in biological systems such as oxygen transport, synthesis of DNA and RNA, hemoglobin formation, and brain and muscle function [1–3]. A deficiency of iron can lead to various biological disorders such as skin alignment, insomnia, anemia, and endotoxemia [4,5]. Moreover, due to the acceleration in industrialization, a lot of iron ion has been emitted in the environment, which is consumed by the human body through edible materials. Thus, iron overload can lead to hepatic cirrhosis, hereditary hemochromatosis leading to neuroinflammation, diabetes, heart failure, and Alzheimer’s disease progression [6–8]. This has prompted the development of different methods for detecting Fe³⁺ ion, such as inductively coupled plasma atomic emission spectrometry, spectrophotometry, atomic absorption spectrophotometry, and electrochemical methods [9]. However, these traditional methods are expensive, less selective, complicated, time consuming, and less sensitive.

Pyrophosphate (PPi) is the dimeric form of the inorganic phosphate and an essential by-product of ATP’s cellular hydrolysis. The concentration of PPi in the cellular system helps us to detect a large number of diseases [10]. The amount of PPi in the cell acts as an indicator of cancer research [11].

A high concentration of PPI is detected in patients with calcium pyrophosphate dihydrate crystal deposition disease (CPPD) [12]. Detection of the PPI has additionally been used for the real-time DNA sequencing. Thus, the detection and imaging of PPI are of vital importance in the case of human beings. Compared to the conventional detection methods for both the ions, fluorescence chemosensors offer a more straightforward and economical method with immense accuracy, sensitivity, and selectivity for the ions' online monitoring.

Metal–Organic Frameworks (MOFs) are extended crystalline structures with high, tunable porosity and surface area that have been widely used for the capture and storage of different gases such as hydrogen, carbon dioxide, and methane [13,14]. Fluorescent chemosensors based on luminescent MOFs have been extensively used for the highly sensitive detection of analytes. The extensive surface area and open avenues in the MOFs allow the fast diffusion of specific analytes for highly sensitive fluorescence detection. These pore environments can be easily tuned using functionalized linkers that provide highly accessible interactional sites and enclosed environments for the highly selective recognition of specific analytes [15,16]. Moreover, the MOF's profound crystalline nature helps understand the host–guest interaction within the MOF and the mechanism of fluorescence [17]. The high oxidation state of Zirconium (IV) leads to enhanced charge density and bond polarization. That results in a robust metal–ligand bond in all the Zirconium-based MOFs leading to high thermal and chemical stability [18,19]. Moreover, the organic linker (benzene ring) of the UiO-66 can be readily derivatized without disturbing the crystalline structure, the thermal property, or the chemical property of the MOF. This particular characteristic of UiO-66 makes it appropriate for different post and pre synthetic modifications. The primary fluorescence in the UiO-66-NH₂ arises from the linker, but due to the zirconium clusters' presence, the emission of the linker is quenched. So, the amino group can be derivatized with different heteroaromatic groups to produce strong emission and strong binding moieties [20,21].

This paper reports the synthesis and characterization of a pyridinyl imine appended UiO-66-NH₂ MOF (UiO-66-N-Py) (Figure 1) and its application in the sequential detection of cation and anion in the aqueous media. A pyridine-imine appended 2-aminoterephthalic acid linker (H₂L) was used to prepare UiO-66-N-Py by the hydrothermal method. Then, the newly synthesized MOF was characterized with powdered XRD, surface area analysis (BET), FTIR, SEM, thermogravimetric analysis (TGA), and the digestion NMR. The fluorescence emission studies with different cations showed that the MOF was highly selective for Fe³⁺, leading to the complete quenching of the fluorescence. Then, this Fe³⁺-incorporated UiO-66-N-Py was used in the same aqueous media for the sequential detection of pyrophosphate anion.

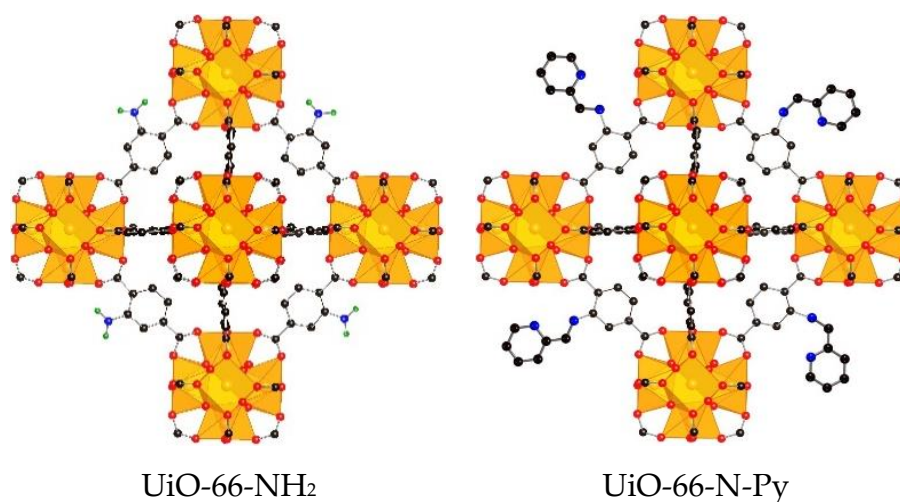


Figure 1. Schematic representation of UiO-66-NH₂ and UiO-66-N-Py.

2. Experimental

2.1. Materials and General Methods

2.1.1. Chemicals Used in this Work

First, 2 aminoterephthalic acid (98% purity), 2-pyridinecarboxaldehyde (99% purity), methanol (99.9% purity), ethanol (97.2% purity), *N,N*-dimethylformamide (DMF; 99.8% purity), dichloromethane (99.8% extra dry grade), all other nitrates or chlorides of the metal salts, and the tetrabutylammonium or potassium salts of the anions were purchased from Sigma Aldrich (USA) Corporation. NMR solvents: dimethyl sulfoxide- d_6 (DMSO- d_6 ; 99.9% purity) were purchased from Cambridge Isotope. All chemicals were used without further purification. Water used in this work was double distilled and filtered through a Millipore membrane. The solutions of metal ions were prepared from their nitrate, and chloride salts and anions were prepared from their tetrabutylammonium or potassium salts (analytical grade) followed by subsequent dilution of the working solutions.

2.1.2. Instrumentation

^1H and ^{13}C NMR spectra were recorded on a Bruker AM-400 spectrometer (Billerica, MA, USA) using Me_4Si as the internal standard. Elemental microanalyses (EA) were performed using a PerkinElmer-EA 2400 elemental analyzer (Waltham, MA, USA). Powdered X-ray diffraction patterns of the samples were recorded using a Rigaku MiniFlex diffractometer (Tokyo, Japan), which was equipped with $\text{Cu-K}\alpha$ radiation. The data were acquired over the 2θ range of 5° and 30° . The FTIR spectra of UiO-66-N-Py were obtained using a Nicolet 6700 Thermo Scientific instrument (Waltham, MA, USA) in the range of $400\text{--}4000\text{ cm}^{-1}$, using KBr. Thermogravimetric analysis (TGA) of the samples were performed using a TA Q500. In this study, an activated UiO-66-N-Py (10 mg) sample was heated in an alumina pan under airflow (60 mL min^{-1}) with a gradient of $10\text{ }^\circ\text{C min}^{-1}$ in the temperature range of $30\text{--}800\text{ }^\circ\text{C}$. The BET surface areas of the MOFs were calculated by using Micromeritics ASAP 2020 instrument (Norcross, GA, USA). These materials' surface morphology was discerned using a field emission scanning electron microscope (FESEM, LYRA 3 Dual Beam, Tescan), which operated at 30 kV. The FESEM samples were prepared from suspension in ethanol. The surface chemical analyses were performed using an XPS equipped with an $\text{Al-K}\alpha$ micro-focusing X-ray monochromator (ESCALAB 250Xi XPS Microprobe, Thermo Scientific, Waltham, MA, USA). Inductively Coupled Plasma Mass Spectrometry (ICP-MS) of the iron ion-treated samples of UiO-66-N-Py were carried in Thermo Scientific X Series 2 ICP-MS. The absorption spectra of the MOF were studied using a Jasco V-670 spectrophotometer (Tokyo, Japan). Fluorescence spectra were measured using a Jasco, FP-8500ST fluorescence spectrophotometer, which was equipped with a xenon discharge lamp and 1 cm quartz cells with slit width 2 nm for both the source and the detector. The quantum yield and chromaticity studies were done using an integration sphere (Jasco FP-8500ST) by using a liquid sample holder at room temperature. The excitation wavelength used in the absolute emission quantum yield measurement is 340 nm, which does not interfere with the emission spectrum, and the concentration is adjusted so that the optical density is 0.1 at the excitation wavelength.

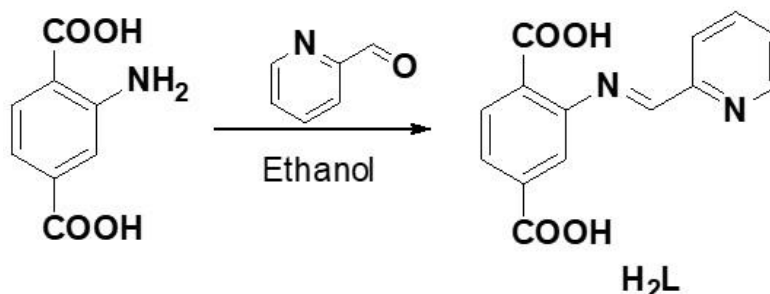
2.1.3. Sample Preparation for Photophysical Studies

In a typical luminescence-sensing experimental setup, 1 mg of UiO-66-N-Py powder was dispersed in 1 mL of water. In a 1 cm quartz cuvette, 3 mL of dispersed aqueous solution of UiO-66-N-Py was placed, and the absorption and emission responses were measured in situ after an incremental addition of freshly prepared analyte solutions. The mixtures were sonicated for 5 min after each incremental addition of the analytes for uniform dispersion during the luminescent measurements. All of the measurements were performed at 298 K. All the optical sensing experiments were carried out using 10^{-2} M aqueous solution of the analyte salt.

2.2. Synthesis

2.2.1. Synthesis of the Linker

The synthesis of the Linker is shown in Scheme 1.



Scheme 1. Synthesis of the linker H_2L .

2.2.2. Synthesis of Compound H_2L

To a solution of 2-aminoterephthalic acid (500 mg, 2.8 mmol) in ethanol (10 mL), 2-pyridinecarboxaldehyde (450 mg, 4.2 mmol) was added and refluxed for 6 h. The reaction mixture was cooled down, and the precipitate was filtered and washed with ethanol to give H_2L as yellow solid in 91% yield. 1H NMR (DMSO- d_6) δ 7.22–7.31 (m, 3H), 7.51 (s, 1H), 7.65 (d, $J = 7.6$ Hz, 1H), 7.76 (d, $J = 8.4$ Hz, 1H), 7.93 (d, $J = 3.2$ Hz, 1H), 8.82 (s, 1H); ^{13}C NMR (DMSO- d_6) δ 108.35, 110.44, 113.03, 113.39, 115.30, 118.09, 125.07, 127.28, 130.99, 132.26, 147.04, 156.57, 162.96, 164.94; Anal. Calcd for $C_{14}H_{10}N_2O_4$: C, 62.22; H, 3.73; N, 10.37; Found: C, 62.18; H, 3.66; N, 10.30 (Figures S1 and S2, in Supplementary Materials).

2.2.3. UiO-66-NH₂

UiO-66-NH₂ was synthesized by dissolving $ZrCl_4$ (250 mg, 1.08 mmol) and 2-amino-1,4-benzenedicarboxylic acid (268 mg, 1.5 mmol) in DMF (40 mL) with ultrasonic vibration for 30 min; then, 0.3 mL of acetic acid was added. The as-obtained mixture was transferred to a 50 mL vial and heated at 393 K for 24 h. Then, the vial was cooled in the air to room temperature. The resulting UiO-66-NH₂ was washed three times with DMF (5–10 mL) using a centrifuge (10,000 rpm for 30 min), and then sequentially immersed in methanol (5–10 mL three times per day) for three 24 h periods. Finally, UiO-66-NH₂ was activated by removing the solvent under vacuum for 24 h at 100 °C. FTIR (KBr, cm^{-1}): 3429, 1663, 1569, 1437, 1382, 1258, and 1094 (Figure S3, Supplementary Materials). Anal. Calcd for $C_{54}H_{52}N_8O_{36}Zr_6$ ($Zr_6O_4(OH)_4(2-NH_2BDC)_6(DMF)_2(H_2O)_2$): C, 33.49; H, 2.71; N, 5.79; Zr, 28.27; Found: C, 33.61; H, 2.99; N, 6.05; Zr, 28.54.

2.2.4. UiO-66-N-Py

UiO-66-N-Py was synthesized in a similar way as above by dissolving $ZrCl_4$ (250 mg, 1.08 mmol) and H_2L (405 mg, 1.5 mmol) in DMF (20 mL) with ultrasonic vibration for 30 min; then, 0.3 mL of acetic acid was added. The as-obtained mixture was transferred to a 50 mL vial and heated at 393 K for 24 h. Then, the vial was cooled in the air to room temperature. The resulting UiO-66-N-Py was washed in the same way as the previous method by three times with DMF (5–10 mL) using a centrifuge (10,000 rpm for 30 min) and then sequentially immersed in methanol (5–10 mL three times per day) for three 24 h periods. Finally, UiO-66-N-Py was activated by removing the solvent under vacuum for 24 h at 110 °C. FTIR (KBr, cm^{-1}): 3093, 1671, 1596, 1521, 1408, 1295, 1227, 1160, and 851 (Figure S3, Supplementary Materials). Anal. Calcd for $C_{90}H_{70}N_{14}O_{36}Zr_6$ ($Zr_6O_4(OH)_4(2-N-Py-BDC)_6(DMF)_2(H_2O)_2$): C, 43.75; H, 2.86; N, 7.94; Zr, 22.15; Found: C, 43.91; H, 2.56; N, 8.17; Zr, 22.55.

3. Results and Discussion

3.1. Characterization of H_2L

In a covalent post-synthetic modification (PSM), there are chances that all the linkers are not completely functionalized within the MOF framework; hence, in this paper, we presynthetically modified the linker 2-amino-terephthalic acid with 2-pyridinylcarboxyaldehyde to give the imine conjugate H_2L (Scheme 1). The structure of H_2L was confirmed with 1H NMR, ^{13}C NMR, (Figures S1 and S2, in Supplementary Materials), and elemental analysis data. The 1H NMR spectra of H_2L exhibited a singlet peak at 8.82 ppm, which corresponds to the imine ($-CH=$) proton, and another doublet peak was noticed at 7.93 ppm that is assigned to the proton adjacent to the nitrogen of the pyridine ring.

3.2. Characterization of $UiO-66-N-Py$ and $UiO-66-NH_2$

The powdered XRD of $UiO-66-NH_2$ was consistent with that reported in the literature (Figure 2) [18]. The high crystalline nature and the peaks of $UiO-66-N-Py$ at $2\theta = 7.78^\circ, 8.92^\circ$ (Figure 2) were found to be consistent with the characteristic peaks of $UiO-66-NH_2$. This establishes that appending 2-aminoterephthalic acid with 2-pyridinylcarboxyaldehyde does not disrupt the framework and connectivity present in $UiO-66-NH_2$.

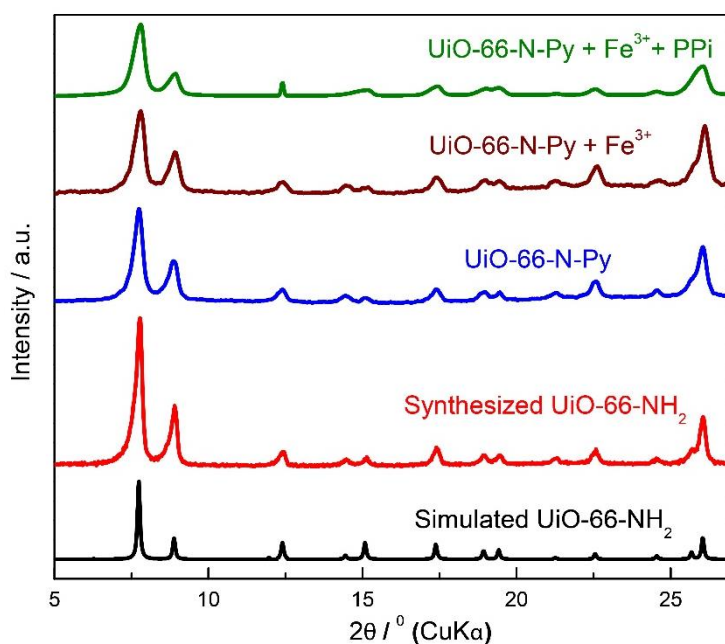


Figure 2. Powdered XRD patterns of $UiO-66-NH_2$ obtained from cif file, $UiO-66-NH_2$ as synthesized, $UiO-66-N-Py$ as synthesized, $UiO-66-N-Py$ after addition of iron, and $UiO-66-N-Py + Fe^{3+}$ after addition of pyrophosphate (PPI).

In the IR spectrum of $UiO-66-N-Py$, the peaks at 1408 cm^{-1} and 1295 cm^{-1} correspond to the carbon–nitrogen bond's vibration in the 2-aminoterephthalate. Similarly, the peaks at 1671 cm^{-1} and 1521 cm^{-1} are assigned to the $-COO$ asymmetrical and symmetrical stretching. The presence of the imine bond in $UiO-66-N-Py$ exhibits a sharp enhanced peak at 1596 cm^{-1} with the disappearance of the N-H stretching peak, which is found in $UiO-66-NH_2$ at the 3429 cm^{-1} (Figure S3, in Supplementary Materials).

The alkaline digestion 1H NMR of $UiO-66-N-Py$ confirmed the presence of the linker H_2L in the framework. The 1H NMR spectrum obtained after the digestion of $UiO-66-N-Py$ has peaks at the chemical shifts analogous to H_2L (Figure S1, in Supplementary Materials).

The N_2 adsorption isotherm of UiO-66-N-Py indicated Type I behavior with a sharp uptake at a very low relative pressure (P/P_0) of 0 to 0.05, which signifies its microporous nature similar to the UiO-66-NH₂. From the isotherm of UiO-66-N-Py, the BET surface area and pore volume were found to be 573 m²g⁻¹ and 0.381 cm³g⁻¹, respectively, which is diminished significantly from the pristine UiO-66-NH₂ (BET surface area = 1032 m²g⁻¹ pore volume = 0.517 cm³g⁻¹) due to the presence of the functionalized pyridine moieties (Figure 3). Furthermore, the DFT adsorption pore-size distribution affirmed a pore diameter of 10.2 Å for UiO-66-N-Py, which is much more reduced than the UiO-66-NH₂ (11.5 Å), indicating the presence of conjugated pyridine groups (Figure S4, in Supplementary Materials).

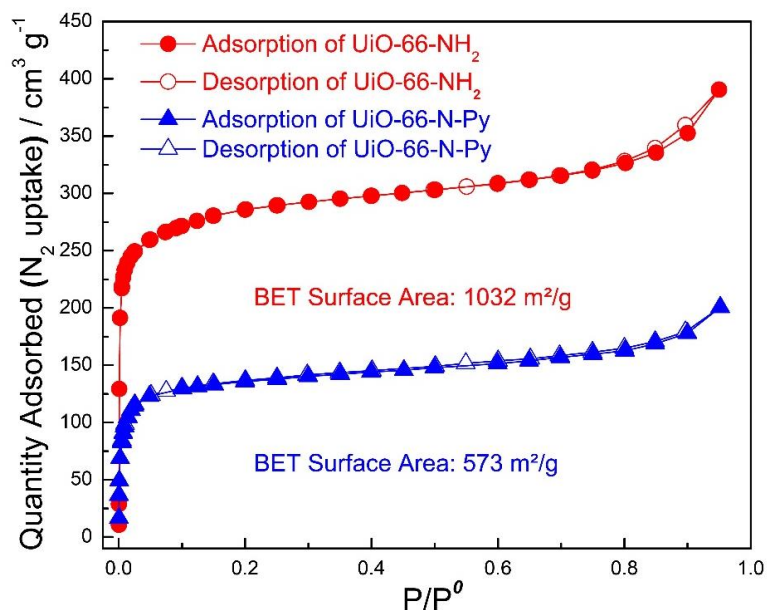


Figure 3. N_2 adsorption isotherms of UiO-66-N-Py and UiO-66-NH₂. The filled and open circles represent the adsorption and desorption branches, respectively.

The thermogravimetric analysis (TGA) was used to study the thermal stability of UiO-66-N-Py and UiO-66-NH₂ materials under an airflow with a heating rate of 5 °C min⁻¹ (Figure 4).

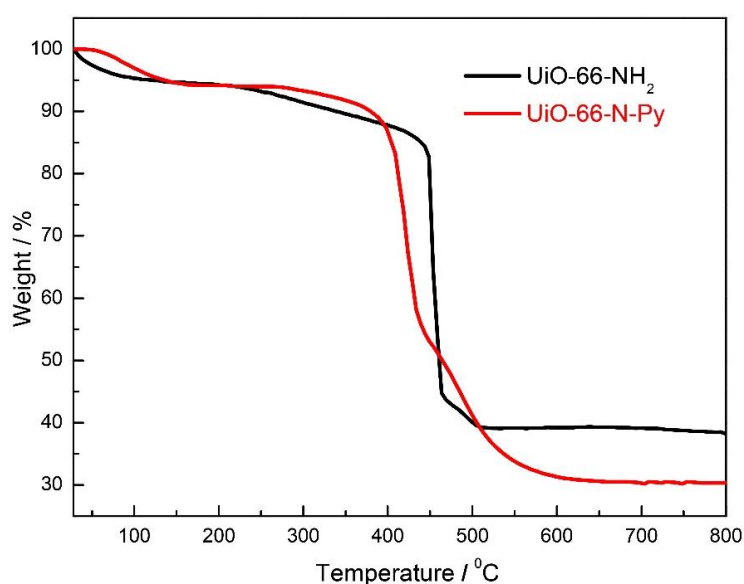


Figure 4. Thermogravimetric analysis (TGA) of UiO-66-N-Py and UiO-66-NH₂.

Both the materials show analogous thermal behavior with an initial mass loss of 5.0% between 200 and 250 °C due to the removal of the trapped solvents molecules from the framework's pores. The maximum weight loss in UiO-66-N-Py is 64.5% at a temperature of 375 °C, indicating the decomposition of the framework. In UiO-66-NH₂, the maximum weight loss of 56.4% occurs at a temperature of 410 °C. It signifies that UiO-66-NH₂ and UiO-66-N-Py are stable up to 375 °C and 410 °C, respectively. The remaining residue of 30.5% for UiO-66-N-Py and 38.6% for UiO-66-NH₂ corresponds to zirconium oxide. Thus, the TGA of the materials illustrates that functionalization with 2-pyridinecarboxaldehyde does not affect the stability of the MOF. The thermal stability of UiO-66-N-Py has also been confirmed by powdered XRD (Figure S5, in Supplementary Materials).

The SEM study of UiO-66-N-Py confirmed that it has uniformly distributed bipyramidal morphology with the particle size ranging from 130 to 150 nm (Figure S6, in Supplementary Materials).

3.3. Optical Properties of UiO-66-N-Py

The photophysical properties of UiO-66-N-Py were investigated as emulsion in an aqueous medium. The comparative absorption spectroscopy of all the linkers, UiO-66-NH₂, and UiO-66-N-Py, indicates that conjugation with pyridine redshifts the absorption peak of UiO-66-NH₂ from 360 to 370 nm in UiO-66-N-Py (Figure S7, in Supplementary Materials). In general, 2-aminoterphthalate is luminescent, but in case of UiO-66-NH₂ ($\lambda_{em} = 449$ nm), due to coordination with the Zr-O clusters, ligand-to-metal charge transfer (LMCT) takes place, and the luminescence is abated [20]. However, in case of UiO-66-N-Py, the emission peak appears at 485 nm on excitation at 341 nm wavelength (Figure S8, in Supplementary Materials). Thus, an enhanced 36 nm redshift in the emission peak of UiO-66-N-Py is produced due to the pyridine ring's conjugation to the 2-aminobenzene ring of the main framework of UiO-66-NH₂. Furthermore, the pyridine group's nitrogen and the imine bond contribute selective binding sites for transitional metal ions. The absolute quantum yield of UiO-66-N-Py, which was calculated from the integrated sphere, was found to be 0.43. The CIE coordinates obtained from the chromaticity diagram were commensurate with the experimentally derived emission peak values (Figure S9, in Supplementary Materials).

3.4. Cation Sensing Properties of UiO-66-N-Py

The cation sensing properties of UiO-66-N-Py were studied by screening with various cations, and the transition in their photophysical properties was noted. It was observed that on the addition of different cations to the aqueous solution of the UiO-66-N-Py, only the Fe³⁺ ion produce a change in the absorbance of UiO-66-N-Py (Figure S10, in Supplementary Materials). On the gradual addition of Fe³⁺ ion to a suspension of UiO-66-N-Py, the absorbance peak at 370 nm diminishes with the formation of a new peak at 315 nm and isobestic point 341 nm (Figure S11, in Supplementary Materials). This formation of a new peak at 315 nm indicates the coordination of the Fe³⁺ with the imine N and the nitrogen of the pyridine. The stoichiometric ratio of binding between the Fe³⁺ and UiO-66-N-Py was validated by Job's plot, which indicated that the complexation between Fe³⁺ and UiO-66-N-Py has a 1:1 stoichiometric ratio (Figure S12, in Supplementary Materials) [22,23].

The chemosensing behavior of UiO-66-N-Py was interpreted by studying the change in fluorescence emission of this MOF with an increasing concentration of Fe³⁺ at an excitation wavelength of 341 nm. The fluorescence emission was significantly quenched with the increasing concentration of Fe³⁺, and a complete quenching was accomplished when the molar ratio of UiO-66-N-Py: Fe³⁺ was 1:1 (Figure 5). This quenching of emission indicates that complete complexation has occurred between the Fe³⁺, imine linkage, and the pyridine moiety. Fe³⁺ being paramagnetic impedes the intramolecular charge transfer from the pyridine ring to the benzene ring of the main structural framework of UiO-66 (Scheme 2), leading to the complete emission suppression. The quenching efficiency indicated by the Stern–Volmer constant (K_{sv}), which is calculated from the fluorescence titration experiment shown in Figure 5, was found to be 1.4×10^5 M⁻¹ (Figure S13, in Supplementary Materials) [24].

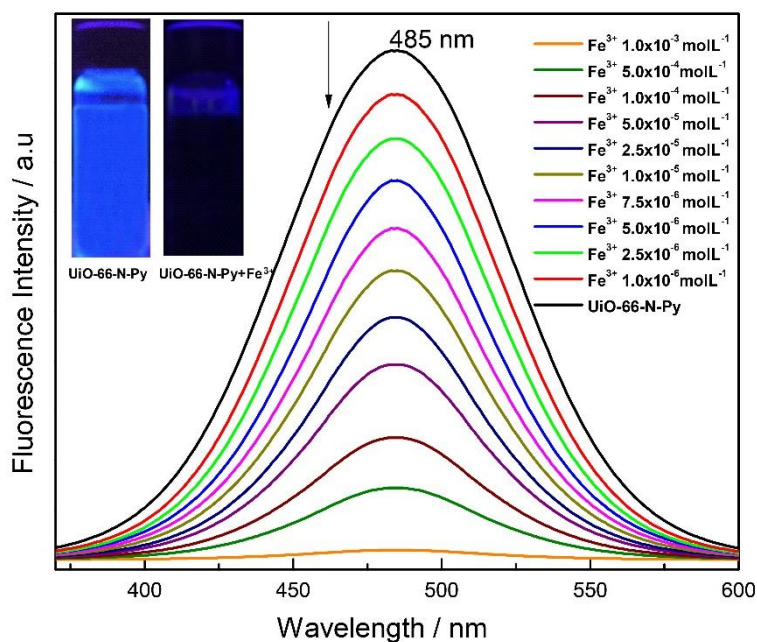
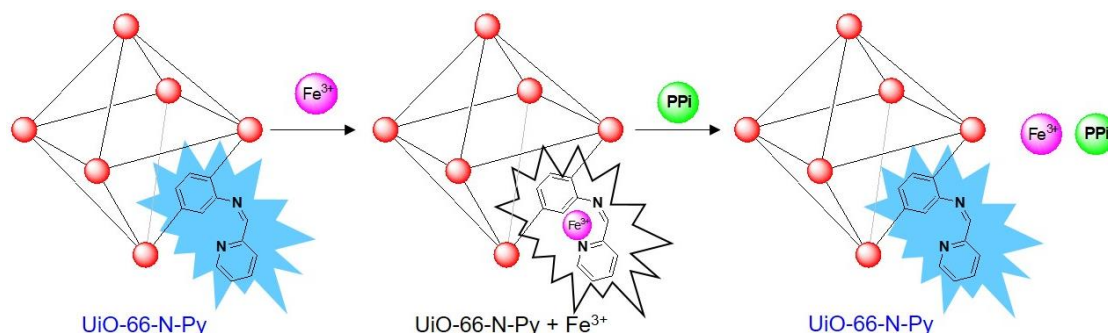


Figure 5. Changes in fluorescence emission spectra of UiO-66-N-Py with the incremental addition of FeCl_3 (10^{-2} M) in water ($\lambda_{\text{exc}} = 341$ nm). Inset: Fluorogenic changes in UiO-66-N-Py upon addition of Fe^{3+} in water upon illumination at 365 nm.



Scheme 2. Schematic illustration of the mechanism of sequential detection of Fe^{3+} and PPI by UiO-66-N-Py.

The sensitivity of UiO-66-N-Py for Fe^{3+} was established from the limit of detection, which was calculated to be 10 ppb ($0.19 \mu\text{M}$) by the ratio of $3\sigma/k$ (Section S6, Table S1, and Figure S24, in Supplementary Materials). The selectivity and the tolerance of UiO-66-N-Py for Fe^{3+} as compared to other metal pollutants was examined by immersion of the MOF into aqueous solution of various metal ions (e.g., Fe^{2+} , Fe^{3+} , Co^{2+} , Cu^{2+} , Ni^{2+} , Zn^{2+} , Cd^{2+} , Hg^{2+} , Ag^+ , Pd^{2+} , Al^{3+} , Ga^{3+} , Pb^{2+} , Na^+ , K^+ , Ca^{2+} , Mg^{2+} , Sr^{2+} , Rb^{2+} , and Cs^{2+}) (Figure 6, and Figure S14 in Supplementary Materials). It was observed that complete emission suppression occurs only in the case of Fe^{3+} due to its paramagnetic nature, and proximity of the pyridine nitrogen with the imine group helps in selective binding of the Fe^{3+} as compared to the other cations [25]. PXRD of UiO-66-N-Py bounded with Fe^{3+} indicated that the framework's crystallinity is not disturbed (Figure 2). Competitive binding experiments with 200 μL of various metal ions along with 200 μL of Fe^{3+} was performed, and it showed that complete quenching of UiO-66-N-Py by Fe^{3+} was not hindered by any of the metal ions (Figure S15, in Supplementary Materials).

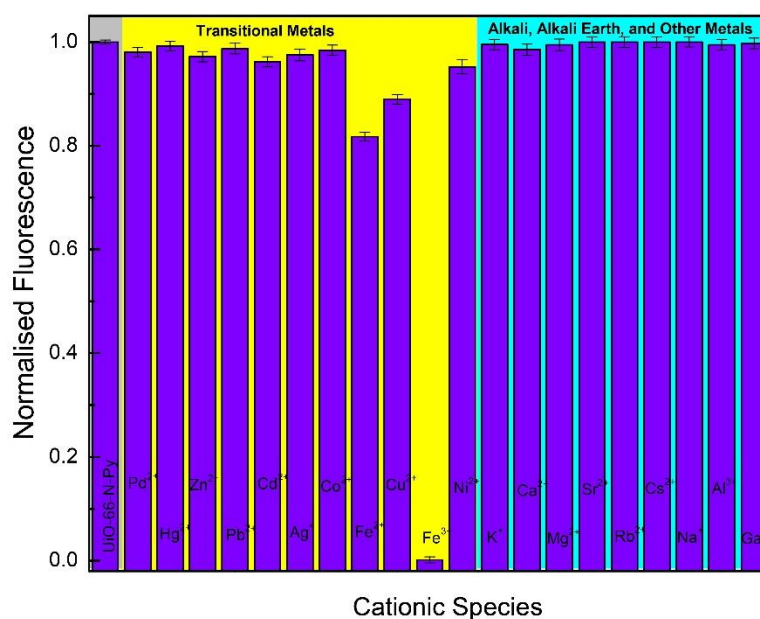


Figure 6. Change in the normalized fluorescence emission of UiO-66-N-Py in water upon the addition of 200 μL of different metal cations (10^{-2} M).

The complexation of Fe^{3+} with UiO-66-N-Py was further confirmed by ICP, FTIR, and the XPS studies of the washed and dried samples. The ICP analysis of the sample confirmed Fe along with the metal of the MOF framework. It was analyzed that 11.891 mg of Fe^{3+} was obtained per 100 mg of the zirconium. The FTIR study of the UiO-66-N-Py samples collected after the sensing experiments provided us essential insight into the nature of the complexation between the guest (Fe^{3+}) and the host framework. The Fe^{3+} ion's complexation with the pyridine nitrogen of UiO-66-N-Py is depicted by the change of the $-\text{C}=\text{N}-$ stretching vibration from 1296 to 1282 cm^{-1} . The Fe^{3+} ion also interacts with the imine linkage of UiO-66-N-Py, which is mirrored by the change in $-\text{C}=\text{N}-$ stretching vibration from 1595 to 1583 cm^{-1} (Figure S16, in Supplementary Materials). In addition, the interaction with Fe^{3+} changes the pyridine's C-H vibration from 3100 to 3067 cm^{-1} (Figure S17, in Supplementary Materials). The XPS of the pristine MOF sample and after complexation with the Fe^{3+} were also analyzed. It was observed that both the MOF indicates the characteristic peaks for C, N, and Zr at 283, 398, and 181 eV, respectively. In UiO-66-N-Py and the Fe^{3+} complex, we can detect peaks for iron at 712 and 726 eV, which emphasized the complexation of UiO-66-N-Py with Fe^{3+} (Figure S18, in Supplementary Materials).

3.5. Anion Sensing Properties of UiO-66-N-Py

It has already been reported that many metal complexes have an affinity toward selective anions such as Ni-CN, Al-F, or Cu-S [26–30]. Thus, we also tried to check the selectivity of different anions F^- , Cl^- , Br^- , I^- , CH_3COO^- , NO_3^- , SO_4^{2-} , HSO_4^- , PO_4^{3-} , ATP, ADP, MnO_4^- , CrO_4^{2-} , $\text{Cr}_2\text{O}_7^{2-}$, and PPI toward the complex of UiO-66-N-Py + Fe^{3+} (Figure 7). Upon the addition of aqueous solution (10^{-2} M) of each anion, there was no change in the emission of UiO-66-N-Py + Fe^{3+} complex except in the case of PPI, where the emission peak of the pristine UiO-66-N-Py was restored at the 485 nm at an excitation wavelength of 341 nm (Figure S19, in Supplementary Materials). The absorbance study also shows that the peak at 315 nm due to Fe^{3+} complexation gradually reduces, and the peak of UiO-66-N-Py is restored at 370 nm (Figure S20, in Supplementary Materials).

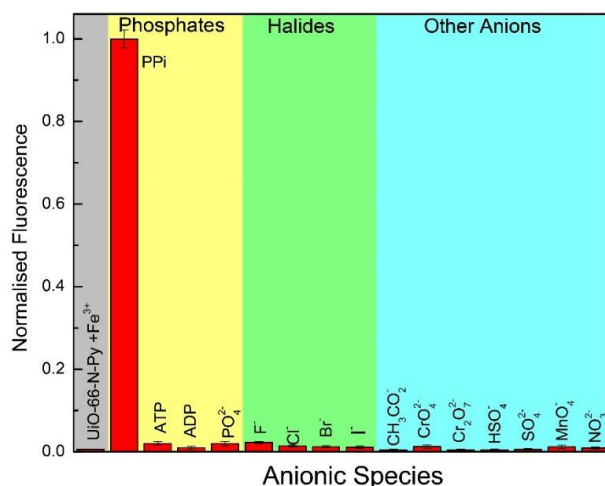


Figure 7. Change in the normalized fluorescence emission of UiO-66-N-Py + Fe³⁺ in water upon addition of 200 μ L of different anionic species (10^{-2} M).

Fluorescence titration of the UiO-66-N-Py + Fe³⁺ complex with the incremental addition of PPI resulted in the enhancement of the emission at 485 nm (Figure 8), with a binding constant of 1.7×10^5 M⁻¹ (Figure S21, in Supplementary Materials). The limit of detection for PPI calculated from the ratio $3\sigma/k$ was estimated to be 50 ppb (0.3 μ M) (Section S6, Table S1, and Figure S25 in Supplementary Materials). Job's method, obtained from the fluorescence emission, established that the stoichiometry of binding of PPI with UiO-66-N-Py + Fe³⁺ is 1:1 (Figure S22, in Supplementary Materials). To delve into the possibility of using UiO-66-N-Py + Fe³⁺ for the practical detection of PPI, competitive binding experiments with different anions (10^{-2} M) in the presence of PPI were carried out. This study showed that the fluorescence enhancement of UiO-66-N-Py + Fe³⁺ by PPI was not interfered by any of the anions (Figure S23, in Supplementary Materials). The FTIR data also show that the interaction of UiO-66-N-Py + Fe³⁺ with PPI shifts the peak of imine stretching and C-H vibration of pyridine from 3067 to 3100 cm⁻¹ (Figures S16 and S17, in Supplementary Materials). An efficient chemosensor for successful practical applications should be effective in aqueous media within a broad pH range. The fluorescence emission of UiO-66-N-Py remained impervious within a pH range of 4.0–8.0 (Figure S26, in Supplementary Materials), even after its regeneration with PPI. Beyond this range, the fluorescence emission properties were lost, which was probably due to breaking the imine linkage or destruction of the UiO-66-N-Py framework.

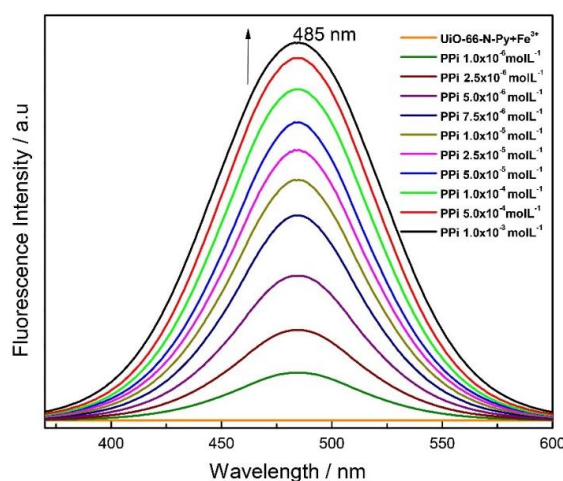


Figure 8. Changes in fluorescence emission spectra of UiO-66-N-Py + Fe³⁺ with the incremental addition of PPI (10^{-2} M) in water ($\lambda_{\text{exc}} = 341$ nm).

The fluorescent enhancement mechanism was due to the release of Fe^{3+} from the UiO-66-N-Py + Fe^{3+} complex by the metal–MOF displacement method by PPI (Scheme 2) [31–33]. This was confirmed by the restoration of the emission peak of the pristine UiO-66-N-Py at 485 nm after interaction with PPI. The PXRD data also confirmed that the crystallinity of the UiO-66-N-Py is intact after the interaction with the PPI (Figure 2).

For this sensor's practical application, a fluorescence test paper was prepared for the portable and straightforward optical sensing of Fe^{3+} . A filter paper of the size $4.0 \times 2.0 \text{ cm}^2$ was immersed in an emulsion of UiO-66-N-Py and water and then dried to get the test paper. As shown in Figure 9, the test paper containing UiO-66-N-Py produces a blue fluorescence that can be seen with the naked eye when placed under UV light irradiation of 365 nm (Figure 9A).

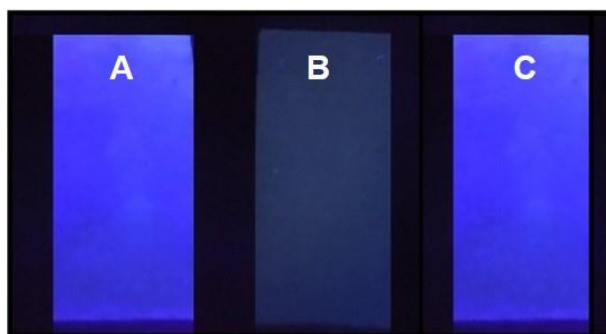


Figure 9. Luminescence picture of the UiO-66-N-Py test paper: (A) UiO-66-N-Py, (B) UiO-66-N-Py + Fe^{3+} (10^{-2} M), (C) UiO-66-N-Py + Fe^{3+} + PPI under UV-light irradiation of 365 nm.

When this test paper is immersed in Fe^{3+} solution and then irradiated by UV light of 365 nm, the fluorescence is completely quenched (Figure 9B). After further immersion of the same quenched test paper into a PPI solution, the blue fluorescence emission is restored (Figure 9C).

3.6. Reusable Properties of UiO-66-N-Py

The recyclable sensing ability of UiO-66-N-Py was measured by repeating the fluorescence sensing experiments with Fe^{3+} and PPI sequentially. The material obtained after the first experiment was washed with water and methanol and then dried at $110 \text{ }^\circ\text{C}$ for 5 h. The recovered UiO-66-N-Py showed an identical change in the emission intensities and sensitivities toward the detection of analytes for six consecutive cycles (Figure 10).

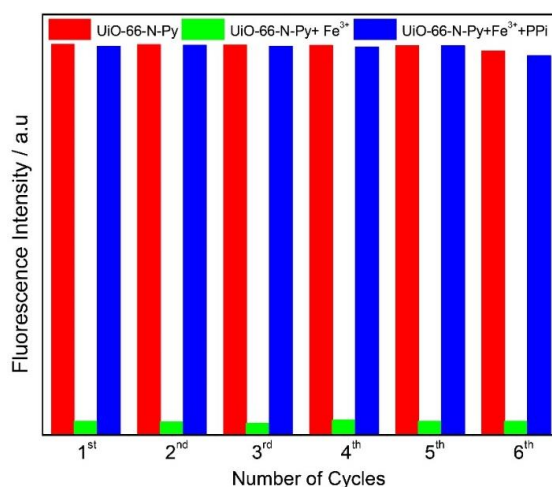


Figure 10. Bar diagram depicting the recyclability of UiO-66-N-Py, fluorescence quenching with UiO-66-N-Py + Fe^{3+} , regeneration of fluorescence with UiO-66-N-Py + Fe^{3+} + PPI up to 6 cycles.

4. Conclusions

In summary, we synthesized an isoreticular MOF UiO-66-N-Py by using a pyridine appended new linker **H₂L**. This presynthetic incorporation of pyridine moiety through imine linkage enhanced the MOF's intrinsic emission property and introduced additional coordinating sites for selective and sensitive binding of Fe³⁺. All the experimental data highlight that UiO-66-N-Py can be used to detect Fe³⁺ ion and the sequential detection of PPI with high efficiency, sensitivity, and selectivity. The detection limits for Fe³⁺ ion and PPI were found to be 10 ppb and 50 ppb, respectively. We investigated the nature of the interaction between the analytes and the functionalized linker of the framework. We also discovered that UiO-66-N-Py has good recyclability for six consecutive cycles without decreasing its sensing performance. Further work related to the sensing of Fe³⁺ in wastewater and the biological application of this sensor is currently being carried out in our lab.

Supplementary Materials: The following are available online at <http://www.mdpi.com/2227-9040/8/4/122/s1>, Figure S1. ¹H NMR spectrum of **H₂L** in DMSO-*d*₆ solution at 400 MHz, Figure S2. ¹³C NMR spectrum of **H₂L** in DMSO-*d*₆ solution at 400 MHz, Figure S3. FTIR spectra of UiO-66-N-Py and UiO-66-NH₂, Figure S4. DFT adsorption pore-size distribution of UiO-66-N-Py and UiO-66-NH₂, Figure S5. Thermal stability of UiO-66-N-Py at different temperatures, Figure S6. SEM image of UiO-66-N-Py, Figure S7. UV-vis spectra of UiO-66-N-Py, UiO-66-NH₂, linkers, and FeCl₃ in water, Figure S8. The fluorescence emission spectra of UiO-66-NH₂ and UiO-66-N-Py. (λ_{ex} = 341 nm), Figure S9. Chromaticity diagram of UiO-66-N-Py dispersion in water, Figure S10. Change in the normalized absorbance of UiO-66-N-Py at 315 in water upon addition of 200 μL of different metal cations (10⁻² M), Figure S11. Changes in UV-vis spectra of UiO-66-N-Py with the incremental addition of FeCl₃ (10⁻² M) in water, Figure S12. Job's plot for UiO-66-N-Py with FeCl₃ in water, Figure S13. Stern-Volmer plot of UiO-66-N-Py quenched by FeCl₃ in water, Figure S14. Changes in emission spectra of UiO-66-N-Py upon addition of 200 μL of different metal cations (10⁻² M) in water. (λ_{ex} = 341 nm), Figure S15. Competitive metal ion selectivity of UiO-66-N-Py: Bars indicate the fluorescence intensity (341 nm excitation, 485 nm emission). Salts of various metal ions (10⁻² M) were added to UiO-66-N-Py and Fe³⁺ (10⁻² M) (a) UiO-66-N-Py only, (b) Ag⁺ + Fe³⁺, (c) Pb²⁺ + Fe³⁺, (d) Zn²⁺ + Fe³⁺, (e) Mg²⁺ + Fe³⁺, (f) Fe³⁺ + Cu²⁺, (g) K⁺ + Fe³⁺, (h) Co²⁺ + Fe³⁺, (i) Al³⁺ + Fe³⁺, (j) Fe²⁺ + Fe³⁺, (k) Na⁺ + Fe³⁺, (l) Cd²⁺ + Fe³⁺, (m) Sr²⁺ + Fe³⁺, (n) Rb⁺ + Fe³⁺, (o) Pd²⁺ + Fe³⁺ (p) Ni²⁺ + Fe³⁺, (q) Hg²⁺ + Fe³⁺, (r) Ga³⁺ + Fe³⁺, (s) Cs⁺ + Fe³⁺, (t) Ca²⁺ + Fe³⁺ in water., Figure S16. Part of FTIR spectra for UiO-66-N-Py before and after sensing experiments with Fe³⁺, Figure S17. Part of FTIR spectra for UiO-66-N-Py before and after sensing experiments with Fe³⁺ and PPI, Figure S18. XPS of UiO-66-N-Py and UiO-66-N-Py + Fe³⁺, Figure S19. Changes in emission spectra of UiO-66-N-Py – Fe³⁺ upon addition of 200 μL of different anionic species (10⁻² M) in water. (λ_{ex} = 341 nm), Figure S20. Changes in UV-vis spectra of UiO-66-N-Py + Fe³⁺ with the incremental addition of PPI (10⁻² M) in water, Figure S21. Binding constant calculation of UiO-66-N-Py + Fe³⁺ with PPI in water, Figure S22. Job's plot for UiO-66-N-Py + Fe³⁺ with PPI in water, Figure S23. Competitive anion selectivity of UiO-66-N-Py + Fe³⁺: Bars indicate the fluorescence intensity (341 nm excitation, 485 nm emission). Various anions (10⁻² M) were added to UiO-66-N-Py + Fe³⁺ and PPI (10⁻² M) (a) UiO-66-N-Py + Fe³⁺ only, (b) F⁻ + PPI, (c) Cl⁻ + PPI, (d) Br⁻ + PPI, (e) I⁻ + PPI, (f) CH₃CO₂⁻ + PPI, (g) MnO₄⁻ + PPI, (h) NO₃²⁻ + PPI, (i) PO₄²⁻ + PPI, (j) SO₄²⁻ + PPI, (k) HSO₄⁻ + PPI, (l) Cr₂O₇²⁻ + PPI, (m) CrO₄²⁻ + PPI, (n) ADP + PPI, (o) ATP + PPI in water, Figure S24. Linear region of fluorescence intensity (λ_x = 341 nm and λ_{em} = 485 nm) for UiO-66-N-Py suspensions in water upon incremental addition of Fe³⁺ solutions, Figure S25. Linear region of fluorescence intensity (λ_{ex} = 341 nm and λ_{em} = 485 nm) for UiO-66-N-Py+Fe³⁺ suspensions in water upon incremental addition of PPI solutions, Table S1. Calculation of the Limit of Detection (LOD), Figure S26. Effect of pH on the emission intensities at 485 nm of UiO-66-N-Py, in H₂O (λ_{ex} = 341 nm).

Author Contributions: Conceptualization, A.H.; methodology, A.H.; formal analysis, A.H., M.E.A., and M.M.R.; investigation, A.H., M.E.A., and M.M.R.; resources, A.H., M.E.A., and M.M.R.; data curation, A.H., and M.E.A.; writing—original draft preparation, A.H.; writing—review and editing, A.H., and M.M.R.; visualization, A.H. and M.M.R.; supervision, A.H.; project administration, A.H.; funding acquisition, A.H. All authors have read and agreed to the published version of the manuscript.

Funding: This research was supported by King Abdulaziz City for Science and Technology—National Science, Technology, and Innovation Plan (NSTIP No. 15-NAN4601-04).

Acknowledgments: We acknowledge King Abdulaziz City for Science and Technology—National Science, Technology, and Innovation Plan (NSTIP No. 15-NAN4601-04) for supporting this research.

Conflicts of Interest: The authors declare no conflict of interest.

References

1. Liu, J.Q.; Li, G.P.; Liu, W.C.; Li, Q.L.; Li, B.H.; Gable, R.W.; Hou, L.; Batten, S.R. Two Unusual Nanocage-Based Ln-MOFs with Triazole Sites: Highly Fluorescent Sensing for Fe^{3+} and Cr_2O_2^- , and Selective CO_2 Capture. *ChemPlusChem* **2016**, *81*, 1299–1304. [[CrossRef](#)]
2. Yan, W.; Zhang, C.; Chen, S.; Han, L.; Zheng, H. Two Lanthanide Metal–Organic Frameworks as Remarkably Selective and Sensitive Bifunctional Luminescence Sensor for Metal Ions and Small Organic Molecules. *ACS Appl. Mater. Interfaces* **2017**, *9*, 1629–1634. [[CrossRef](#)] [[PubMed](#)]
3. Dang, S.; Ma, E.; Sun, Z.-M.; Zhang, H. A layer-structured EuMOF as a highly selective fluorescent probe for Fe^{3+} detection through a cation-exchange approach. *J. Mater. Chem.* **2012**, *22*, 16920–16926. [[CrossRef](#)]
4. Zhao, D.; Liu, X.-H.; Zhao, Y.; Wang, P.; Liu, Y.; Azam, M.; Al Resayes, S.I.; Lu, Y.; Sun, W.-Y. Luminescent Cd(II)–organic frameworks with chelating NH_2 sites for selective detection of Fe (III) and antibiotics. *J. Mater. Chem. A* **2017**, *5*, 15797–15807. [[CrossRef](#)]
5. Gogoi, C.; Yousufuddin, M.; Biswas, S. A new 3D luminescent Zn(II)-organic framework containing a quinoline-2,6-dicarboxylate linker for the highly selective sensing of Fe(III) ions. *Dalton Trans.* **2019**, *48*, 1766–1773. [[CrossRef](#)]
6. Andrews, N.C. Disorders of iron metabolism. *N. Engl. J. Med.* **1999**, *341*, 1986–1995. [[CrossRef](#)] [[PubMed](#)]
7. Omar, F.O.; Blakley, B.R. Vitamin E is protective against iron toxicity and iron-induced hepatic vitamin E depletion in mice. *J. Nutr.* **1993**, *123*, 1649–1655. [[CrossRef](#)] [[PubMed](#)]
8. Muñoz, M.; García-Erce, J.A.; Remach, A.F. Disorders of iron metabolism. Part II: Iron deficiency and iron overload. *J. Clin. Pathol.* **2011**, *64*, 287–296. [[CrossRef](#)]
9. Rath, B.B.; Vittal, J.J. Water Stable Zn(II) Metal–Organic Framework as a Selective and Sensitive Luminescent Probe for Fe(III) and Chromate Ions. *Inorg. Chem.* **2020**, *59*, 8818–8826. [[CrossRef](#)]
10. Lee, S.; Yuen, K.K.Y.; Jolliffe, K.A.; Yoon, J. Fluorescent and colorimetric chemosensors for pyrophosphate. *Chem. Soc. Rev.* **2015**, *44*, 1749–1762. [[CrossRef](#)]
11. Timms, A.E.; Zhang, Y.; Russell, R.G.G.; Brown, M.A. Genetic studies of disorders of calcium crystal deposition. *Rheumatology* **2002**, *41*, 725–729. [[CrossRef](#)]
12. Xu, S.; He, M.; Yu, H.; Cai, X.; Tan, X.; Lu, B.; Shu, B. A quantitative method to measure telomerase activity by bioluminescence connected with telomeric repeat amplification protocol. *Anal. Biochem.* **2001**, *299*, 188–193. [[CrossRef](#)] [[PubMed](#)]
13. Li, H.; Wang, K.; Sun, Y.; Lollar, C.T.; Li, J.; Zhou, H.C. Recent advances in gas storage and separation using metal-organic frameworks. *Mater. Today* **2018**, *21*, 108–121. [[CrossRef](#)]
14. Ataalla, M.; Mohamed, A.; Ali, M.A.; Hassan, M.; Hamad, N.; Afify, A.S. WO_3 -Based Glass-Crystalline Sensor for Selective Detection of Ammonia Gas. In *Nanoscience and Nanotechnology in Security and Protection against CBRN Threats. NATO Science for Peace and Security Series B: Physics and Biophysics*; Petkov, P., Achour, M., Popov, C., Eds.; Springer: Dordrecht, The Netherlands, 2020. [[CrossRef](#)]
15. Zhao, Y.; Yang, X.G.; Lu, X.M.; Yang, C.D.; Fan, N.N.; Yang, Z.T.; Wang, L.Y.; Ma, L.F. $\{\text{Zn}_6\}$ Cluster based metal–organic framework with enhanced room-temperature phosphorescence and optoelectronic performances. *Inorg. Chem.* **2019**, *58*, 6215–6221. [[CrossRef](#)] [[PubMed](#)]
16. Zhao, Y.; Wang, L.; Fan, N.N.; Han, M.L.; Yang, G.P.; Ma, L.F. Porous Zn(II)-based metal–organic frameworks decorated with carboxylate groups exhibiting high gas adsorption and separation of organic dyes. *Cryst. Growth Des.* **2018**, *18*, 7114–7121. [[CrossRef](#)]
17. Liu, Y.; Xie Cheng, X.-Y.C.; Shao, Z.-S.; Wang, H.-S. Strategies to fabricate metal–organic framework (MOF)-based luminescent sensing platforms. *J. Mater. Chem. C* **2019**, *7*, 10743–10763. [[CrossRef](#)]
18. Cavka, J.H.; Jakobsen, S.; Olsbye, U.; Guillou, N.; Lamberti, C.; Bordiga, S.; Lillerud, K.P. A New Zirconium Inorganic Building Brick Forming Metal Organic Frameworks with Exceptional Stability. *J. Am. Chem. Soc.* **2008**, *130*, 13850–13851. [[CrossRef](#)]
19. Bai, Y.; Dou, Y.; Xie, L.-H.; Rutledge, W.; Li, J.-R.; Zhou, H.-C. Zr-based metal–organic frameworks: Design, synthesis, structure, and applications. *Chem. Soc. Rev.* **2016**, *45*, 2327–2367. [[CrossRef](#)]
20. Yang, J.; Dai, Y.; Zhu, X.; Wang, Z.; Li, Y.; Zhuang, Q.; Shi, J.; Gu, J. Metal-Organic Frameworks with inherent recognition sites for selective phosphate sensing through their coordination-induced fluorescence enhancement effect. *J. Mater. Chem. A* **2015**, *3*, 7445–7452. [[CrossRef](#)]

21. Helal, A.; Shaikh, M.N.; Aziz, M.A. Dual sensing of copper ion and chromium (VI) oxyanions by benzotriazole functionalized UiO-66 metal-organic framework in aqueous media. *J. Photochem. Photobiol. A* **2020**, *389*, 112238–112245. [[CrossRef](#)]
22. Sanda, S.; Parshamoni, S.; Biswas, S.; Konar, S. Highly Selective Detection of Palladium and Picric Acid by a Luminescent MOF: A Dual Functional Fluorescent Sensor. *Chem. Commun.* **2015**, *51*, 6576–6579. [[CrossRef](#)]
23. Helal, A.; Nguyen, H.L.; Al-Ahmed, A.; Cordova, K.E.; Yamani, Z.H. An Ultrasensitive and Selective Metal-Organic Framework Chemosensor for Palladium Detection in Water. *Inorg. Chem.* **2019**, *58*, 1738–1741. [[CrossRef](#)]
24. Zheng, M.; Tan, H.; Xie, Z.; Zhang, L.; Jing, X.; Sun, Z. Fast Response and High Sensitivity Europium Metal Organic Framework Fluorescent Probe with Chelating Terpyridine Sites for Fe³⁺. *ACS Appl. Mater. Interfaces* **2013**, *5*, 1078–1083. [[CrossRef](#)]
25. Sahoo, S.K.; Crisponi, G. Recent Advances on Iron(III) Selective Fluorescent Probes with Possible Applications in Bioimaging. *Molecules* **2019**, *24*, 3267. [[CrossRef](#)] [[PubMed](#)]
26. Zhang, D.; Jin, W. Highly selective and sensitive colorimetric probe for hydrogen sulfide by a copper(II) complex of azo-dye based on chemosensing ensemble approach. *Spectrochim. Acta Part A* **2012**, *90*, 35–39. [[CrossRef](#)]
27. Liu, H.; Zhang, B.; Tan, C.; Liu, F.; Cao, J.; Tan, Y.; Jiang, Y. Simultaneous bioimaging recognition of Al³⁺ and Cu²⁺ in living-cell, and further detection of F⁻ and S²⁻ by a simple fluorogenic benzimidazole-based chemosensor. *Talanta* **2016**, *161*, 309–319. [[CrossRef](#)] [[PubMed](#)]
28. Aulsebrook, M.L.; Biswas, S.; Leaver, F.M.; Grace, M.R.; Graham, B.; Barrios, A.M.; Tuck, K.L. A luminogenic lanthanide-based probe for the highly selective detection of nanomolar sulfide levels in aqueous samples. *Chem. Commun.* **2017**, *153*, 4911–4914. [[CrossRef](#)] [[PubMed](#)]
29. Kang, J.H.; Lee, S.Y.; Ahn, H.M.; Kim, C. A novel colorimetric chemosensor for the sequential detection of Ni²⁺ and CN⁻ in aqueous solution. *Sens. Actuators B Chem* **2017**, *242*, 25–34. [[CrossRef](#)]
30. Hu, J.; Hu, Z.; Chen, Z.; Gao, H.W.; Uvdal, K. A logic gate based fluorogenic probe for Hg²⁺ detection and its applications in cellular imaging. *Anal. Chim. Acta* **2016**, *919*, 85–93. [[CrossRef](#)]
31. You, G.R.; Jang, H.J.; Jo, T.G.; Kim, C. A novel displacement- type colorimetric chemosensor or the detection of Cu²⁺ and GSH in aqueous solution. *RSC Adv.* **2016**, *6*, 74400–74408. [[CrossRef](#)]
32. Elmas, S.N.K.; Ozen, F.; Koran, K.; Yilmaz, I.; Gorgulu, A.O.; Erdemir, S. Coumarin Based Highly Selective “off-on off” Type Novel Fluorescent Sensor for Cu²⁺ and S²⁻ in Aqueous Solution. *J. Fluoresc.* **2017**, *27*, 463–471. [[CrossRef](#)] [[PubMed](#)]
33. Liu, X.; Ngo, H.T.; Ge, Z.; Butler, S.J.; Jolliffe, K.A. Tuning colourimetric indicator displacement assays for naked-eye sensing of pyrophosphate in aqueous media. *Chem. Sci.* **2013**, *4*, 1680–1686. [[CrossRef](#)]

Publisher’s Note: MDPI stays neutral with regard to jurisdictional claims in published maps and institutional affiliations.



© 2020 by the authors. Licensee MDPI, Basel, Switzerland. This article is an open access article distributed under the terms and conditions of the Creative Commons Attribution (CC BY) license (<http://creativecommons.org/licenses/by/4.0/>).